Chapter 7

Formation of metal-enriched 2nd generation objects

7.1 Summary

In this chapter we discuss very preliminary results concerning the dispersal of metals into the IGM and nearby halos from two representative Population III supernovae: a 30 $M_\odot$ star with an explosion energy of $E_{SN} = 1.2 \times 10^{51}$ ergs, and a 250 $M_\odot$ star with an explosion energy of $E_{SN} = 8 \times 10^{52}$ ergs. Despite the amount of gas in the Population III halo and the relatively high density of the IGM at $z \simeq 18$, the explosion of the 30 $M_\odot$ star spread metals over a region several hundred proper parsecs in radius within fifty million years. The simulation of the supernova from the 250 $M_\odot$ star is ongoing, but due to the preprocessing of the halo in which the star forms by the star's HII region and the much higher explosion energy suggests that the more massive star will spread metals over a much larger volume of space.

7.2 Motivation

Observations of quasar absorption spectra show that the universe at the present day is uniformly polluted with metals, even at the lowest observed column densities, which correspond to regions of very low overdensity which are know as the Lyman-α forest [84, 85]. The primordial composition of the universe is well understood, and post-BBN nucleosynthesis is believed to take place only in stars and cataclysmic events associated with them. Because of this, it is apparent that this period of enrichment must have taken place between the epoch of first star formation and the present day.

The metals produced by Population III supernovae would have a very important effect on the following generations of stars. The addition of metals greatly enhances the cooling

properties of the gas – molecular hydrogen is a relatively poor coolant compared to dust grains and metal-based molecules such as CO, both of which are produced in significant quantities by both primordial Type II supernovae and pair-instability supernovae, with the fractional quantity of dust increasing as the stellar mass increases [89, 90, 91]. Very little metal is required for gas to cool efficiently – analytical work and simulations suggest that the presence of carbon and oxygen at levels $10^{-4} - 10^{-3}$ $Z_{\odot}$ would be sufficient for enhanced fragmentation of collapsing gas clouds, signifying a change from the top-heavy Population III IMF to a mass function resembling that observed in the galaxy today [93, 94]. As with their HII regions, the metals ejected from Population III supernovae, particularly if the stars fall into the mass range that produces highly energetic pair-instability supernovae, can propagate to great distances – simulations indicate that the ejecta from a massive PISN can eject metal into a sphere of ~ 1 kpc diameter at $z \sim 20$, producing a metallicity floor above that needed for enhanced cooling to take place [95]. However, these calculations were done using SPH calculations with poor spatial and mass resolution, and cannot accurately resolve such important properties such as the degree to which the supernova ejecta mixed with the primordial gas and also the dispersion of metallicities in the enriched gas. Furthermore, previous calculations did not follow the ejected gas to the point where the metals reached nearby halos, and due to their use of SPH, even if they did allow the calculation to progress for a long enough time they would not have been able to make any statements about the degree to which metals may have enriched nearby halos.

This chapter presents very preliminary results from two calculations done with the Enzo AMR code (described in detail in Chapter 2). These calculations are of the explosions of two Population III stars: one with a mass of 30 $M_{\odot}$ and an explosion energy of 1.2×10^{51} ergs (corresponding to the Population III equivalent of a standard Type II supernova), and a second with a mass of 250 $M_{\odot}$ and an explosion energy of 8×10^{52} ergs (corresponding to a massive pair-instability supernova). These two calculations bracket the plausible range of Population III supernova energies presented by Heger et al. [60, 61]. The purpose of the calculations is to model the ejection of metals from these representative Pop III supernovae into the IGM and to follow the mixing history of the supernova ejecta. The ultimate goal is to predict the overall dispersal of metals into the IGM by these stars, and also to attempt to understand the formation site of the first generation of metal-enriched stars.

7.3 Problem setup

In order to obtain the initial conditions for our supernova calculations, we perform a standard Population III star formation calculation, as described in detail in Chapter 4. This calculation was set up in a 0.3 h^{-1} Mpc box, as described in Section 4.3, with

identical cosmological parameters, initialization strategy, and spatial and mass resolution. In this calculation we use the ZEUS hydro method (Section 2.2.3) instead of the PPM method (Section 2.2.2) because it is more stable in situations where the overall pressure jump between adjacent cells is extremely high. This does not change the results of the star formation calculation appreciably. The simulation was followed until $z \simeq 18$, at which point the halo core collapsed and began to form a Population III protostar. At this point, we stop the calculation and put a Pop III supernova into the calculation by hand in the simulation volume and the simulation is then allowed to continue.

The 30 $M_\odot$ supernova is set up as follows: We assume that the evolution of the star along the main sequence occurs much more rapidly than the evolution of cosmological structure, and place the supernova into the calculation at the redshift at which we stopped the calculation. One dimensional calculations by Dan Whalen (private communication) suggest that in the spherically symmetric case, the HII region produced by a 30 $M_\odot$ primordial star will not escape the halo – it remains as a completely bound HII region with a maximum radius of ~ 0.1 pc (proper). For this reason, we do not concern ourselves with the HII region, since it will not affect the dynamics of the supernova remnant in any significant way. Using the mean density and temperature of the inner few parsecs of the halo at this time, we calculate the Sedov blast profile of the supernova at a radius of 2 proper parsecs assuming $E_{SN} = 1.2 \times 10^{51}$ ergs. The mean density of the inner two parsecs of the halo is $n_{mean} \simeq 1800$ cm^{-3} and the mean temperature is approximately 500 K. At this radius the velocity of the supernova shock is 171 km/s. We assume that the supernova is spherically symmetric, and overlay the Sedov blast profile over the inner two parsecs of the halo, centered on the cell with the highest baryon density at the time of collapse. The calculation is then allowed to evolve for approximately 50 million years, with snapshots of the state of the simulation taken at regular intervals over this time.

The 250 $M_\odot$ supernova is set up in a somewhat different way. One dimensional calculations by Whalen, Abel and Norman [76] show that in the spherically symmetric case the HII region from a 250 $M_\odot$ primordial star will extend out to several proper kiloparsecs at $z = 20$, and additionally the increase in gas pressure in the cosmological halo will cause most of the gas in the halo to be ejected by the end of the main sequence lifetime of the star. At the end of the star's life, this gas will be in a thick, dense shell at roughly the virial radius with a velocity of approximately 30 km/s, which is roughly a factor of ten greater than the halo's escape velocity. Due to this, we set up our supernova calculation assuming that the 250 $M_\odot$ supernova goes off within a HII region which is set up using an identical method to that described in Section 6.3. We then calculate the Sedov blast profile of a supernova with $E_{SN} = 8 \times 10^{52}$ ergs exploding in an ambient medium with a density of $\simeq 0.4$ cm^{-3} and a temperature of 17,000 K, which is approximately the mean density and temperature of the gas left over in the halo by the HII region at the end of the star's main sequence lifetime. At this density, the supernova will sweep up its own mass of gas in the ambient medium at $r \simeq 20$ pc (which

is approximately the mass scale at which it makes the transition from the free-expansion to Sedov-Taylor phase), and will not encounter significant density increases until the gas reaches ~ 60 pc. We somewhat arbitrarily decide to put the Sedov profile in with a radius of 40 proper parsecs. At this radius the supernova explosion is propagating outward at a speed of $\simeq 1800$ km/s.

Both supernova calculations are then restarted, assuming a maximum refinement level of 10 (corresponding to a spatial resolution of approximately 0.17 proper parsecs at $z = 18$) and allowed to continue until the velocity of the supernova ejecta drops below the sound speed of the ambient medium, which approximately corresponds to the point at which the supernova ejecta and ambient medium reach pressure equilibrium. This takes slightly more than fifty million years for the 30 $M_\odot$ calculation. At the time that this chapter is being written the 250 $M_\odot$ calculation has not yet been completed, since the overall computational cost is much greater, due to the higher shock velocities and hotter average temperature of the ambient medium due to the HII region. Therefore, we only present results from the 30 $M_\odot$ supernova calculation below.

7.4 Preliminary results

Due to time constraints, only very preliminary results are presented in this chapter. Figures 7.1 and 7.2 show the evolution of the supernova remnant over approximately 60 million years. Figure 7.1 shows the evolution of the remnant over approximately the first half million years after the supernova occurs. In this figure, the left, center and right columns show the initial conditions for our supernova (the Sedov blast profile), 2.68×10^5 years after the initial explosion, and 5.51×10^5 years after the initial explosion, respectively. The rows correspond to (from top to bottom) log baryon density, log metallicity, and log baryon temperature. In all cases the color table is fixed such that all panels in a given row can be directly compared. In the plots of log metallicity the color table spans a range of metallicities from 10^{-4} $Z_\odot$ and below (black, essentially unenriched gas) to 10 times solar metallicity (bright yellow). The majority of gas contained within the actual remnant in the second two timesteps is at a few times solar metallicity. The temperature color table ranges from 100 K (black) to 10^4 K (bright white). The mean temperature of the gas within the supernova remnant at late times is a few thousand K. The box is a projection of a field of view 93 proper parsecs on a side (at $z \simeq 18$) and 93 proper parsecs deep. The development of non-perturbations can be seen very clearly as the supernova remnant expands. Though the initial conditions for the supernova assume spherical symmetry at small scales, inhomogeneities in baryon density outside of the halo core introduce asymmetries which are magnified as the remnant expands, resulting in small "bullets" of gas and significant variations in density, temperature and metallicity in the remnant shell. Unfortunately, some numerical artifacts can be seen –

the supernova remnant shows some signs of a cross-like symmetry, aligned with the grid axes. Most of the "bullets" of high density gas also appear to be preferentially traveling along the axes. The effect is relatively subtle, fortunately, and may not have a significant effect on the results.

Figure 7.2 shows the evolution of the remnant at later times and on a much larger scale. The projected volume is now 1.5 proper kpc on a side and 1.5 proper kpc deep at $z \sim 18$. The columns correspond to (from left to right) 5.51×10^5, 5.79×10^6, and 6.3×10^7 years after the supernova is initialized, respectively. The final timestep corresponds to $z \simeq 15$. The rows and color tables are identical to Figure 7.1. As the supernova remnant expands it becomes less spherically symmetric, eventually becoming pressure-balanced with the IGM after metal has spread several hundred parsecs from the initial halo. Comparison of the leftmost and rightmost columns shows that metal has spread to at least the distance of the nearest neighboring halos, though it is unclear at present how much metal has managed to get to the center of the neighboring halos, where one presumes star formation would take place.

Figures 7.3 and 7.4 show several spherically-averaged, mass weighted baryon quantities as a function of radius. The lines correspond to the five time outputs shown in Figures 7.1 and 7.2. Figure 7.3 shows the number density, enclosed mass, radial velocity and baryon temperature as a function of radius. The shock starts out at $r = 2$ pc with a maximum speed of approximately 100 km/s and an overall temperature of 10^5 K (which is too high to see on this plot). The r^{-2} density profile of the halo can be clearly seen at larger radii. As time goes by, the shock rapidly cools and slows down, and a shell of gas with a thickness of several parsecs forms that is rushing out of the halo. The extreme thickness of this shell may be due to the poor cooling properties of the gas – in this calculation, we assume a primordial cooling function for simplicity. The relatively low molecular hydrogen fraction (discussed below) and temperature ($\sim 10^3$ K) suggest that the gas is not cooling efficiently. The use of a cooling function that assumes a metallicity consistent with that observed in the remnant (also discussed below) would result in much colder gas and presumably a thinner shell. It is also interesting to note the feature in the radial velocity plot at early times where the outgoing gas has a double-peaked profile, with an inner shock that has a slower velocity than the outer one. The inner shock is actually traveling backwards in the rest frame of the main shock, and corresponds to gas which has caught up to the decelerating outer shock and has reflected off of it. This feature is common to calculations of supernova remnant expansion.

Figure 7.4 shows the time evolution of spherically averaged radial profiles of the mass-weighted metallicity and metal dispersion (in units of solar metallicity), as well as the molecular hydrogen mass fraction. In this case what we call the "metal dispersion" is really the square root of the mass-averaged metal dispersion calculated in spherical shells, so that it also has units of solar metallicity (instead of the square of solar metallicity). As one might expect, the metallicity drops rapidly as the remnant expands and mixes with

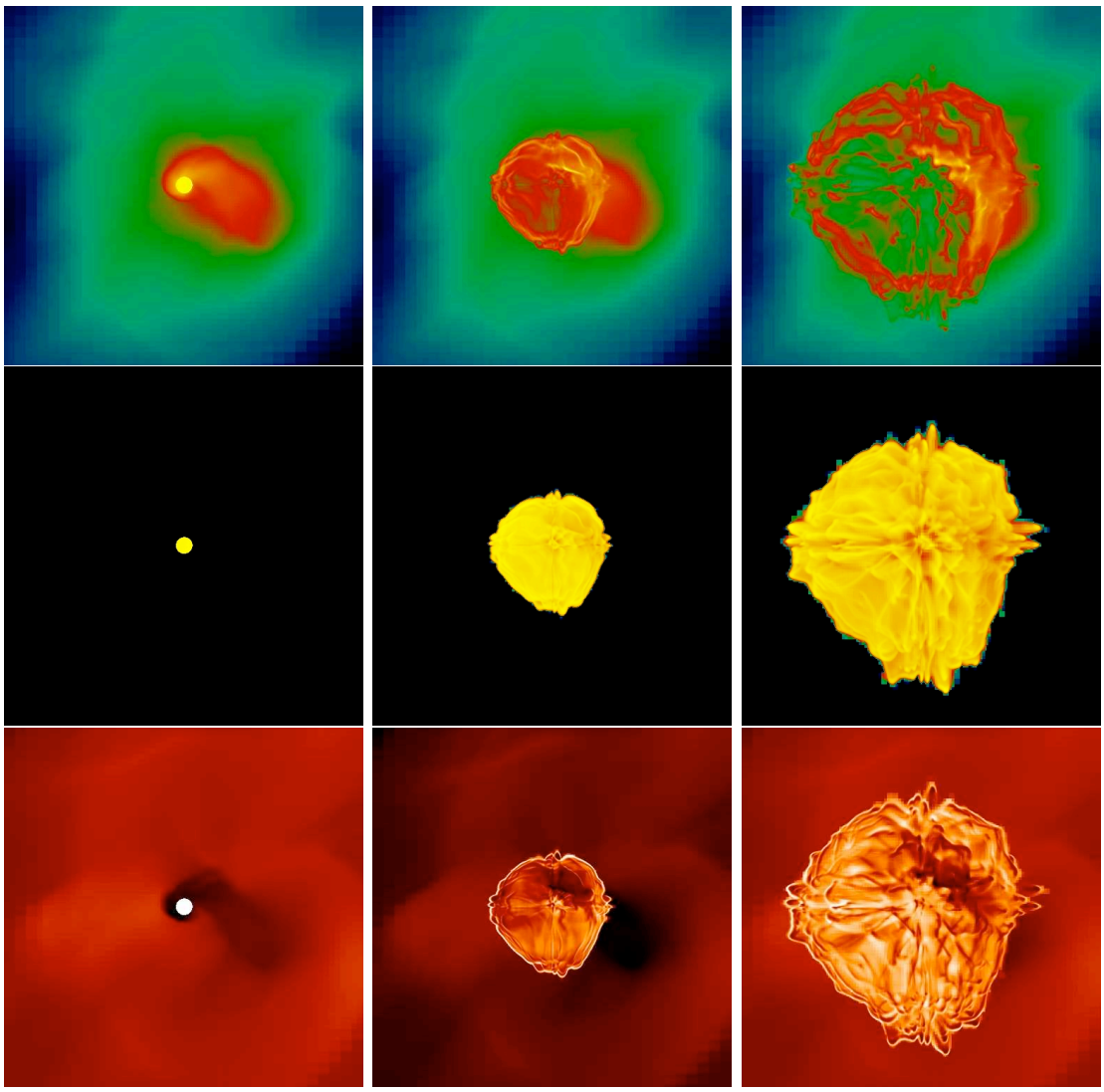

Figure 7.1: Early time evolution of the supernova at $t = t_{SN}$ (left column), $t = t_{SN} + 2.68 \times 10^5$ years (center column) and $t = t_{SN} + 5.51 \times 10^5$ years (right column). Rows correspond to (from top to bottom) projected, mass-weighted baryon density, metallicity, and temperature. The projected region is 93 proper parsecs across at $z \simeq 18$. Images of all quantities have fixed color tables and the columns are directly comparable.

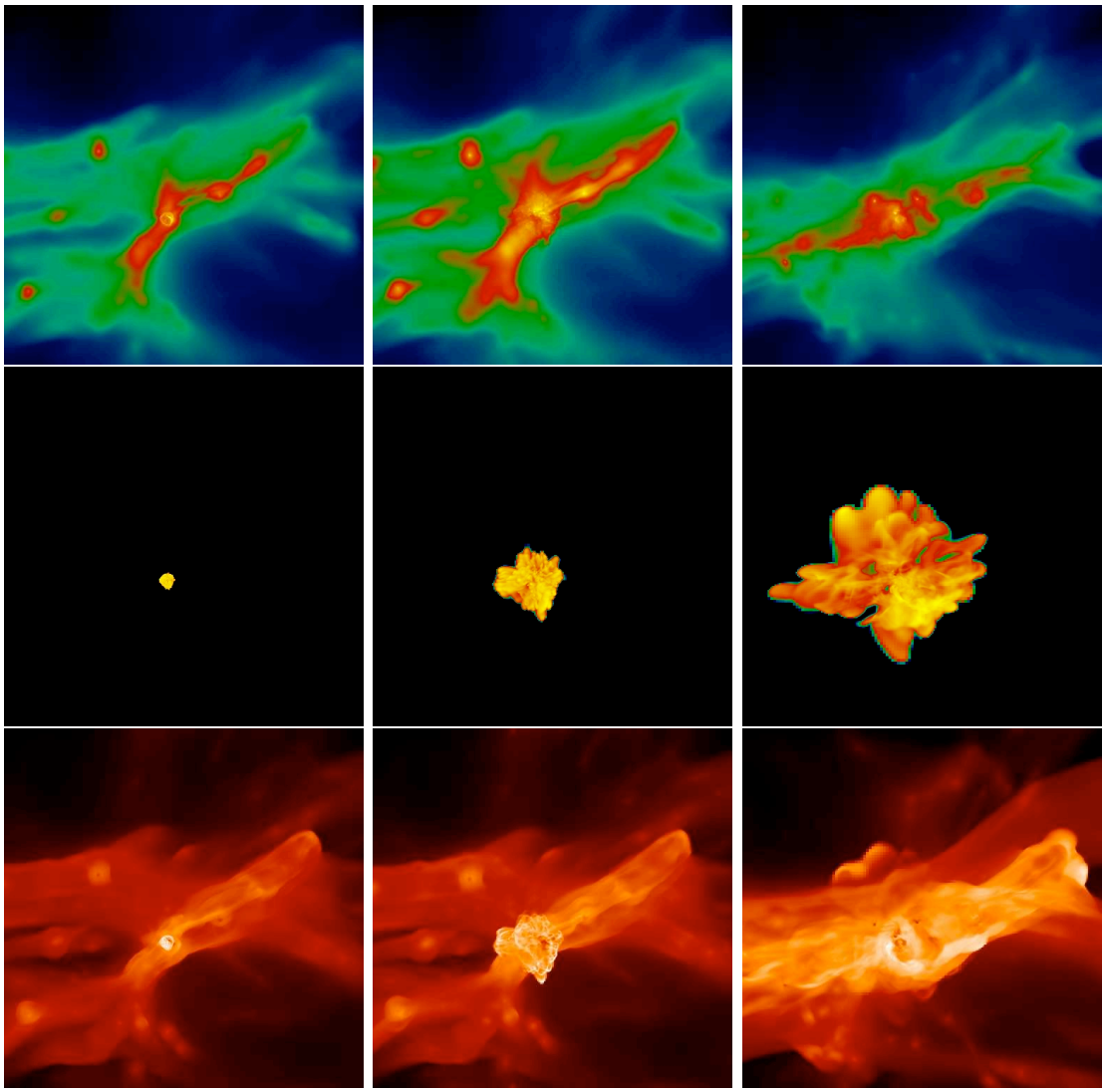

Figure 7.2: Late time evolution of the supernova at $t = t_{SN}+5.51\times10^5$ years (left column), $t = t_{SN} + 5.79 \times 10^6$ years (center column) and $t = t_{SN} + 6.3 \times 10^7$ years later (right column). Rows correspond to (from top to bottom) projected, mass-weighted baryon density, metallicity, and temperature. The projected region is $\simeq 1.5$ proper kiloparsecs across at $z \simeq 18$. Images of all quantities have fixed color tables and the columns are directly comparable.

the pristine gas. However, after the initial time shown the variance of the metallicity remains on the same order of magnitude as the actual metallicity, suggesting that the metallicity of the gas in spherical shells varies strongly, indicating that the gas is poorly mixed. This is clearly true at late times, since the supernova remnant is no longer spherically symmetric.

7.5 Discussion

This chapter presents results from a representative Population III supernova. Two calculations were initialized (supernovae from 30 $M_\odot$ and 250 $M_\odot$ primordial stars) but only the 30 $M_\odot$ case was completed by the time that this thesis was due. The 250 $M_\odot$ is a significantly more costly calculation since the higher temperatures and blast velocities directly correspond to a lower Courant time, making the simulation more than an order of magnitude more expensive overall.

These calculations make several simplifying assumptions that may affect the overall results. In both of the calculations we make the assumption that the supernova remnant is spherically symmetric at the radius at which we put in the Sedov blast profile. While a reasonable assumption for a first calculation of Population III supernovae, this is clearly not true for supernovae from rotating stars, and may affect the overall results. The trend in a rotating star would be towards more metal mixing early in the explosion, resulting in a greater overall distribution of metallicities in the gas polluted by these supernovae, making the scatter in metal distributions in these calculations a lower limit. This being said, the supernovae encounter many thousands of times their own initial mass in gas outside of the radius at which the Sedov profile is put in the gas. This gas is not of uniform composition, and causes a great deal of metal mixing. This can be seen in the figures in Section 7.4, where the remnant shows distinctly non-spherical features and a high degree of metal mixing at both early and late times, so even though the initial setup assumes spherical symmetry the result may not be significantly different than if the initial setup was of an aspherical supernova.

An additional simplifying assumption concerns the cooling rate of the supernova remnant. In this calculation we assume a nonequilibrium primordial chemistry, which predicts a cooling rate that is far lower than that of a metal-enriched gas. This lower cooling rate results in a thicker remnant shell, which then becomes less likely to be affected by the Vishniac instability [227]. This instability is significant in that it can cause fragmentation in the shell of the remnant, which may lead to the development of a second generation of stars which are metal-enriched. This level of fragmentation is not seen in this calculation, due to the choice of cooling function. Future work using simulations whose cooling tables assume metal line cooling will be done, and will show whether this effect is significant.

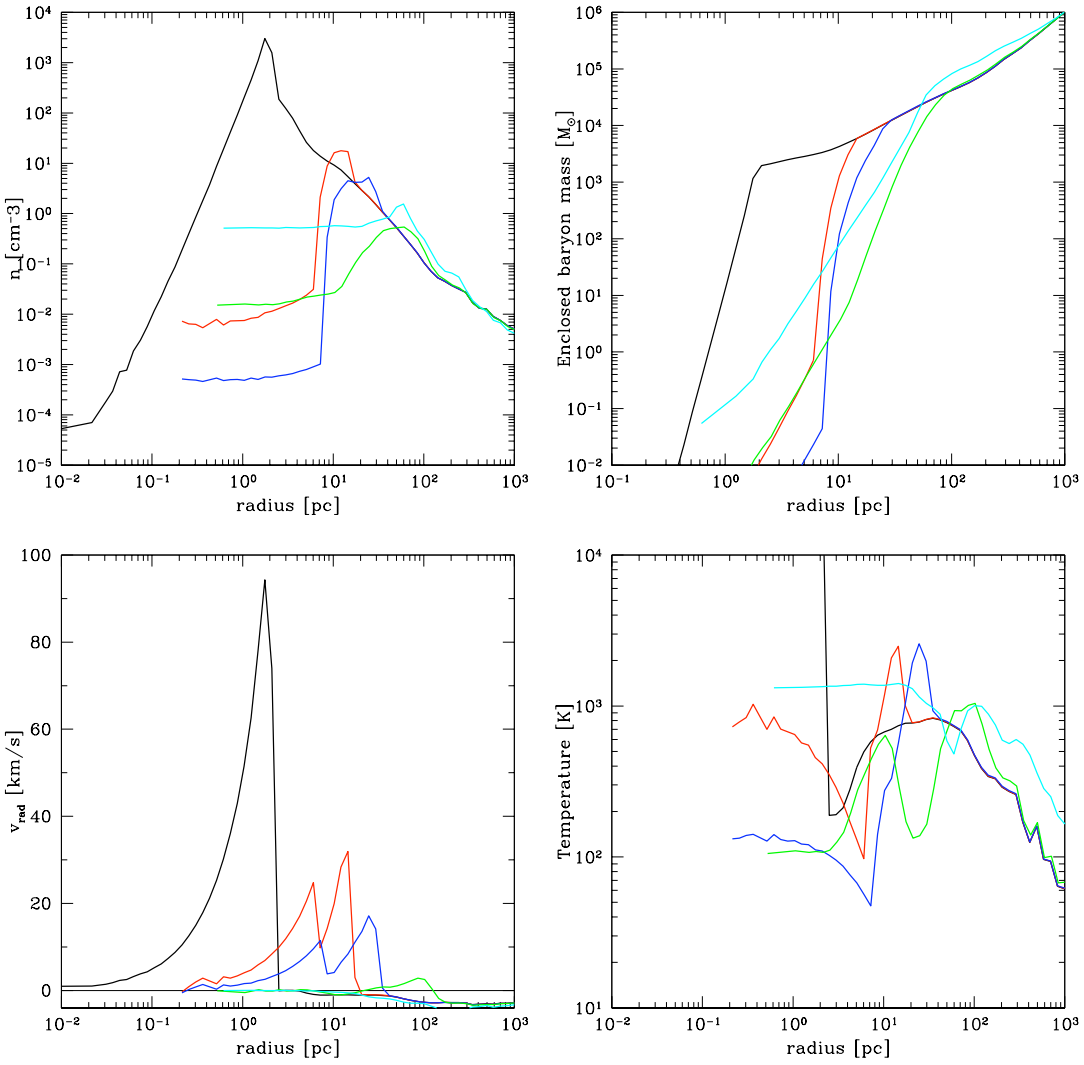

Figure 7.3: Evolution of spherically-averaged, mass weighted baryon properties of the supernova remnant as a function of time. Black line: $t = t_{SN}$. Red line: $t = +2.68 \times 10^5$ years. Blue line: $t = t_{SN} + 5.51 \times 10^5$ years. Green line: $t = t_{SN} + 5.79 \times 10^6$ years. Cyan line: $t = t_{SN} + 6.3 \times 10^7$ years. Top left panel: number density as a function of radius. Top right: enclosed mass as a function of radius. Bottom left: radial velocity as a function of radius. Bottom right: temperature as a function of radius. The x-axis in all plots is identical.

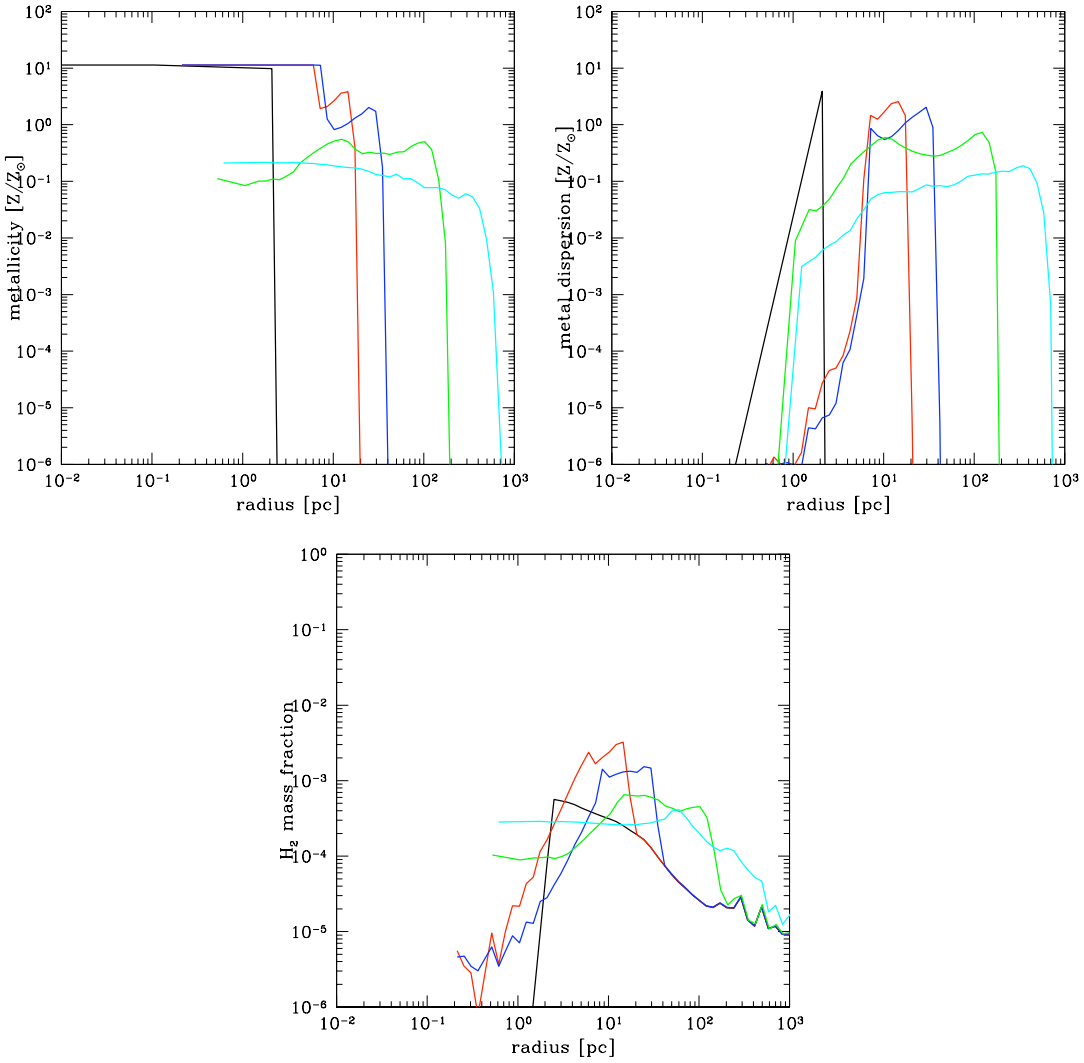

Figure 7.4: Evolution of spherically-averaged, mass weighted baryon properties of the supernova remnant as a function of time. Black line: $t = t_{SN}$. Red line: $t = +2.68 \times 10^5$ years. Blue line: $t = t_{SN} + 5.51 \times 10^5$ years. Green line: $t = t_{SN} + 5.79 \times 10^6$ years. Cyan line: $t = t_{SN} + 6.3 \times 10^7$ years. Top left panel: metallicity (in units of solar metallicity) as a function of radius. Top right: metal dispersion as a function of radius. Bottom: molecular hydrogen mass fraction as a function of radius. The x-axis in all plots is identical.

It is interesting to note that the 30 $M_\odot$ supernova completely disrupts the halo that it occurs in, and drives the majority of the baryons in the halo into the intergalactic medium. This can be understood simply by comparing the energy of the supernova with the binding energy of the halo. The 30 $M_\odot$ supernova has a total energy of 1.2×10^{51} ergs, more than 95% of which is kinetic energy at the time at which the Sedov blast profile is assumed. At this point in time the total mass of the halo is 4.15×10^5 $M_\odot$, with 4.7×10^4 $M_\odot$ of this being in baryons. The virial radius of a halo with this mass is $\simeq 125$ proper parsecs at $z = 18$. Altogether, this corresponds to a binding energy of 7×10^{49} ergs for the entire halo. However, the dark matter does not directly feel the effects of the supernova explosion, so the relevant component of the halo is simply the baryon gas. This component of the halo has a binding energy of approximately 8×10^{48} ergs, which is more than two orders of magnitude less than the supernova explosion energy! This calculation of the binding energy makes the simplifying assumption that the density of the halo is uniform, and somewhat underestimates the overall binding energy of the halo, which has a density profile that scales as r^{-2}. Still, we obtain a reasonable order-of-magnitude estimate that agrees with the simulation results and provides a simple physical understanding of the situation.

The calculations described in this section are considered to be preliminary "scoping" calculations for a more advanced series of simulations involving output from calculations looking at the three-dimensional evolution of supernovae from rotating Population III stars done by Fryer & Rockefeller. Additionally, these calculations will include a cooling table which correctly incorporates cooling due to metal molecules and dust, and will be done at higher spatial resolution to more accurately determine metal mixing in the intergalactic medium and nearby halos, and to examine the formation of the first generation of metal-enriched stars.